

## Modal Analysis of Pressures on a Full-Scale Spinnaker

**Julien Deparday**

Naval Academy Research Institute, Brest, France

**Patrick Bot**

Naval Academy Research Institute, Brest, France

**Frédéric Hauville**

Naval Academy Research Institute, Brest, France

**Benoît Augier**

Naval Academy Research Institute, Brest, France

**Marc Rabaud**

Laboratoire FAST, Univ.Paris-Sud, CNRS, Université Paris-Saclay, F-91405, Orsay, France

**Dario Motta**

University of Auckland, New-Zealand

**David Le Pelley**

University of Auckland, New-Zealand

Manuscript received January 17, 2017; revision received February 13, 2017; accepted March 16, 2017.

**Abstract:** While sailing offwind, the trimmer typically adjusts the downwind sail “on the verge of luffing”, occasionally letting the luff of the sail flap. Due to the unsteadiness of the spinnaker itself, maintaining the luff on the verge of luffing requires continual adjustments. The propulsive force generated by the offwind sail depends on this trimming and is highly fluctuating. During a flapping sequence, the aerodynamic load can fluctuate by 50% of the average load. On a J/80 class yacht, we simultaneously measured time-resolved pressures on the spinnaker, aerodynamic loads, boat data and wind data. Significant spatio-temporal patterns were detected in the pressure distribution. In this paper we present averages and main fluctuations of pressure distributions and of load coefficients for different apparent wind angles as well as a refined analysis of pressure fluctuations, using the Proper Orthogonal Decomposition (POD) method. POD shows that pressure fluctuations due to luffing of the spinnaker can be well represented by only one proper mode related to a unique spatial pressure pattern and a dynamic behavior evolving with the Apparent Wind Angles. The time evolution of this proper mode is highly correlated with load fluctuations. Moreover, POD can be employed to filter the measured pressures more efficiently than basic filters. The reconstruction using the first few modes makes it possible to restrict the flapping analysis to the most energetic part of the signal and remove insignificant variations and noises. This might be helpful for comparison with other measurements and numerical simulations.

**Keywords:** full scale experiment, instrumented boat, spinnaker, fluid structure interaction, POD, unsteady

## NOMENCLATURE

AWA	Apparent Wind Angle [°]
AWS	Apparent Wind Speed [m/s]
BS	Boat Speed [m/s]
$C_F$	Load coefficient [-]
$C_{xy}$	Normalised inter-correlation function of temporal signals $X(t)$ and $Y(t)$ [-]
$f_r$	Reduced frequency [-]
$f_s$	Pseudo frequency of mode time coefficient [Hz]
$P_{leeward}$	Local pressure on the leeward side of the sail [Pa]
$P_{windward}$	Local pressure on the windward side of the sail [Pa]
$S$	Spinnaker surface area [68 m <sup>2</sup> ]
$t$	Time [s]
thres <sub>AWA</sub>	Upper bound of the AWA's standard deviation [°]
thres <sub>AWS</sub>	Upper bound of the AWS' standard deviation [°]
thres <sub>time</sub>	Lower bound of a "stable" period [s]
TWS	True Wind Speed [m/s]
$x$	Coordinate along the longitudinal axis of the boat, positive forward [m]
$y$	Coordinate perpendicular to the boat's symmetry plane, positive port [m]
$z$	Vertical coordinate, positive upwards [m]
$\Delta C_P$	Differential pressure coefficient [-]
$\Delta P$	Differential pressure [Pa]
$\mu_x$	Mean function of signals $X(t)$ [-]
$\mu_y$	Mean function of signals $Y(t)$ [-]
$\rho$	Density of air [1.25 kg/m <sup>3</sup> ]
$\tau$	Non-dimensional time [-]
$\mathbf{a}$	Vector of the POD mode time coefficients [-]
$\mathbf{U}$	Vector input data of the POD [-]
$\mathbf{C}$	Covariance matrix of the POD [-]
$\lambda$	Vector of the POD Eigenvalues [-]
$\Phi$	Vector of the POD Eigenvectors [-]
IQR	Inter Quartile Range (Q3-Q1)
Q1	First Quartile
Q3	Third Quartile
POD	Proper Orthogonal Decomposition

## INTRODUCTION

In research and development in sail aerodynamics, full-scale testing, wind tunnel testing and numerical simulation have always been complementary. Numerical simulations contribute to efficiently investigating different designs without the cost of creating sails (Chapin et al. 2011; Ranzenbach et al. 2013; Durand et al. 2014; Viola et al. 2015). Nowadays, advanced computational resources have enhanced numerical simulation and have allowed coupling of fluid and structural solvers to create Fluid-Structure Interaction simulations (Renzsch and Graf 2010; Chapin et al. 2011; Lombardi et al. 2012; Ranzenbach et al. 2013; Trimarchi et al. 2013; Augier et al. 2014; Durand et al. 2014). However, wind tunnel testing and full-scale

testing are required for comparison and validation (Hansen et al. 2002; Viola and Flay 2011; Renzsch and Graf 2013). Wind tunnel testing has the advantage of being in a controlled environment where a balance can be used to measure the forces created by the sails on the boat frame (Flay 1996; Zasso et al. 2005; Graf and Müller 2009; Campbell 2014b). These results can easily be used to create a Velocity Prediction Program (Le Pelley and Richards 2011; Campbell 2014a). Nevertheless with wind tunnel testing, some rules of similitude are violated such as the Reynolds number, the ratio of fabric weight to wind pressure, or the ratio of membrane stress to wind pressure. Full-Scale testing does not have these issues, and contributes in the determination of yacht performance in real sailing conditions. These experiments require complex set-up in a harsh environment but actual aerodynamic loads can be assessed in a variety of ways. Sail boat dynamometers (Herman 1989; Hochkirch and Brandt 1999; Masuyama 2014) measured forces from upwind sails transmitted to the boat frame. Fossati et al. (2015) created a sail boat dynamometer with the possibility of measuring aerodynamic forces of downwind sails. Augier et al. (2012) carried out experiments where loads on the rigging lines and sails were measured. They contributed to a better understanding of the interaction between the wind, the rigging and the sails. Le Pelley et al. (2015) measured the forces and the directions on the three corners of spinnakers. Viola and Flay (2012), Le Pelley et al. (2012), Lozej et al. (2012), and Motta et al. (2014) measured pressures on sails for upwind and downwind sails.

Downwind sails however are more complex to study than upwind sails mainly due to their non-developable 3D shape with highly cambered sections and massively detached flow around a thin and very flexible membrane. Due to the dynamic behavior of this unsteady fluid-structure interaction, the pressures on the sail vary quickly. Even in stable conditions, offwind sails have an inherent unsteadiness. One key feature of spinnaker unsteadiness comes from the flapping at the leading edge, also called luffing. We have previously investigated pressure evolution during luffing (Deparday et al. 2014; Motta et al. 2015). In Deparday et al. (2014), we showed an example where the flapping of spinnaker creates pressure peaks at the leading edge increasing the aerodynamic force dynamically by 50%. Due to the non-stationarity of the environment while sailing, spatio-temporal pressure data are complex to analyze and therefore to simulate. However significant and different spatio-temporal patterns can be spotted (Motta et al. 2015) and might be produced by different physical causes (Fluid-Structure Interaction, wind variations, boat motions, etc.). In this paper we present an approach to decompose complex pressure evolutions into simpler modes. It would then allow easier analysis and comparison with simulations.

This paper presents results of full-scale experiments of an instrumented J/80 class yacht in offwind conditions where loads, pressures on the spinnaker, boat and wind data were measured. After describing the experimental apparatus, average and fluctuations of pressures and loads are presented. The next section is the use of the Proper Orthogonal Decomposition (POD) method on pressures to create a simpler model of the complex variations of pressure distribution in time. We then show that the method also helps to highlight the correlation between the main evolution of pressures and the variations of loads.

## **EXPERIMENTAL SETUP**

An instrumented J/80 class sailing yacht, an 8 meter one-design cruiser racer is used during these experiments. A tri-radial asymmetrical spinnaker with a surface area of about 68 m<sup>2</sup> with a 12 meter long rounded luff is hoisted as well as a mainsail of 17 m<sup>2</sup>. Boat and wind data, loads on the standing rigging and on the sails are recorded. Pressure taps, developed by the Yacht Research Unit at the University of Auckland are stuck on the spinnaker to acquire the

dynamic pressure distribution. They are synchronized with the other data using an acquisition software, RTMaps developed by Intempora which receives every signal at its own rate and timestamped them “on the flow”. A resampling is applied during the post processing to obtain synchronous data for easier analysis. Figure 1 shows the arrangement of all the sensors set onboard.

This setup for downwind navigation is a further development of the experimental system described in Augier et al. (2012) which was used for measurements in upwind navigation.

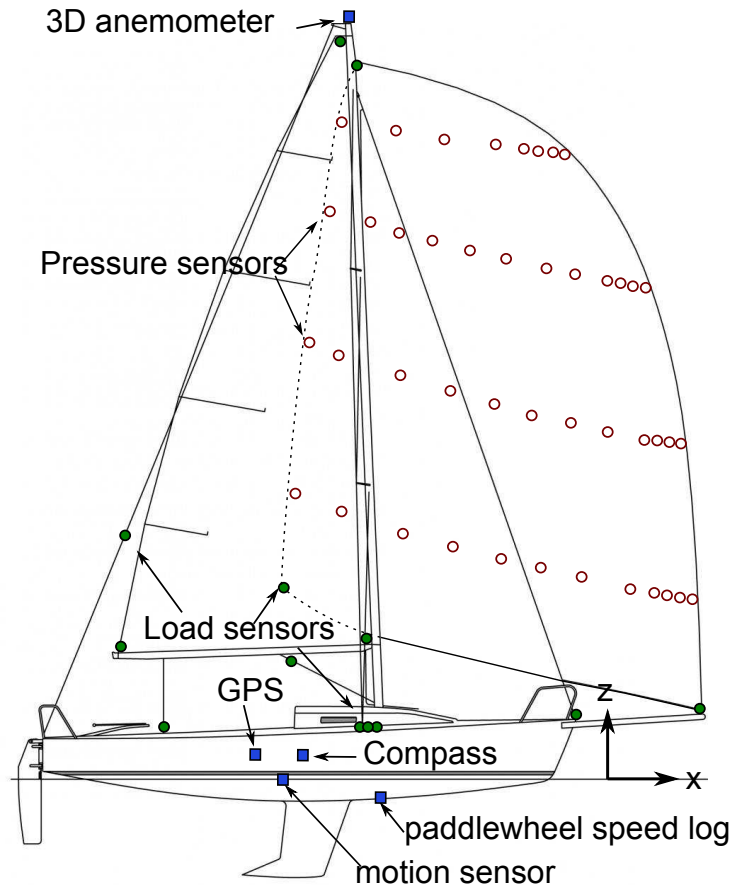


**Figure 1. General arrangement of the experimental set-up on the J/80. 16 load sensors (green discs), 44 pressure taps (red circles), and wind and boat sensors (blue squares).**

## Loads

The standing rigging (shrouds, forestay and backstay) is fitted with custom-made turnbuckles and shackles equipped with strain gages. The running rigging (the corners of the mainsail and of the spinnaker head, tack and clew) is also equipped with instrumented shackles. For the standing rigging and the mainsail the sensors are connected to a load acquisition system Spider8 from HBM. Voltages are received from all strain gages and amplified. They are then converted in digital data at a rate of 25 Hz. Thereafter they are transferred to the real-time acquisition software, RTMaps. Due to the high displacements of the spinnaker (in the order of magnitude of 1 to 5 meters for the spinnaker used in these experiments), the instrumented shackles on the three corners of the spinnaker communicate wirelessly to the acquisition system. The clew sensor is connected via a wire running along the foot of the sail to a small box located near the tack point of the spinnaker (see figure 2). This box contains two strain gage amplifiers, one for the tack sensor and one for the clew. A microcontroller receives and transmits data at a sampling frequency of 25 Hz to the receiver inside the boat via a wireless

and low consumption ZigBee network. Another box is located at the head position for the head-instrumented shackle. The delay between the transmission and reception of data is insignificant compared to dynamics in sailing.

The errors of measurement are less than 2% of the measurement range (10 000 N for the shrouds, forestay and for the mainsail sheet, 5000 N for the backstay and other instrumented shackles on the mainsail and spinnaker).



**Figure 2. Photograph of the spinnaker tack. A: tack shackle wired to the acquisition box. B: wire running along the foot from the clew shackle to acquisition box. C: Acquisition box with strain gauge amplifiers, a microcontroller, a wireless transmitter and a battery.**

### **Pressures on spinnaker**

On the spinnaker, 44 low-range differential pressure sensors (Honeywell XSCL04DC) are located on the surface along 4 horizontal stripes: at 1/4, 1/2, 3/4 and 7/8 height of the spinnaker from the foot (see figures 1 and 2). Twelve transducers are used on each of the first 3 stripes and 8 for the top one. There is a higher concentration of pressure taps near the leading edge to be able to record potential leading edge suction peaks. These sensors measure a difference of pressure between the suction side and the pressure side using the piezoresistive effect. There is no need for a measure of a reference pressure, a complicated task in full-scale experiments. The sensors are stuck on one side (at the pressure side when sailing on portside tack) and are positioned facing 2mm-diameter holes in the sail to measure the pressure jump across the sail without significant air leak. Punctured light sail cloth patches are applied on the pressure taps to improve the aerodynamic profile of the sensors. This custom-built pressure system was designed by the Yacht Research Unit at the University of Auckland. These pressure transducers are connected by wires to the receiver inside the boat and thus are synchronized with the other data. The pressure sensors have a sampling frequency of approximately 10 Hz with a maximum range of  $\pm 1$  kPa and a resolution of 0.5 Pa. The pressure acquisition system is further described in Motta et al. 2014.

### **Procedure**

Sea trials were performed in the bay of Brest, France, offshore from Ecole Navale. During these experiments the weather conditions were stable:

- average true wind speed: 6 m/s (12 kn)

- gust: 8 m/s (16 kn)
- wind direction: 270° (westerly wind). Stable. Flat water.

Even in conditions considered as “stable” (with no gust, no wind shift, on flat water and fixed trimming), offwind sails have an inherent unsteadiness, like luffing (flapping at the leading edge). To keep a “stable condition”, defined by the mean of low standard deviation of the AWA (lower than 4°) and the AWS (lower than 10% of the AWS), a standard procedure must be followed.

Wind is considered as the only input control of the sailing yacht system. The trim and the helm are adjusted as a function of the wind direction and force. The trimmer adjusted the spinnaker at the optimum trim (i.e. on the verge of luffing at the leading edge) and the helmsman kept the apparent wind angle as constant as possible. Trimmer and helmsman were held constant for all the trials. Aerodynamic loads are considered as an output, a response to the environmental conditions.

At full-scale, wind variations cannot be controlled. In order to analyze the intrinsic dynamics of flapping, and not the dynamics of the onset wind flow, “stable” periods are defined according to a “stable” wind that is quantified as follows:

- The standard deviation of the AWA during the “stable” period should not be larger than a threshold  $thres_{AWA}$ .
- The standard deviation of the AWS during the “stable” period should not be larger than a threshold  $thres_{AWS}$ , which is a fraction of the time-averaged AWS
- The “stable” period should last a defined minimum of time:  $\Delta t > thres_{time}$ .

The thresholds used are:

$$\begin{cases} thres_{AWA} = 4^\circ \\ thres_{AWS} = 10\% \text{ of the mean AWS} \\ thres_{time} = 5 \text{ s} \end{cases}$$

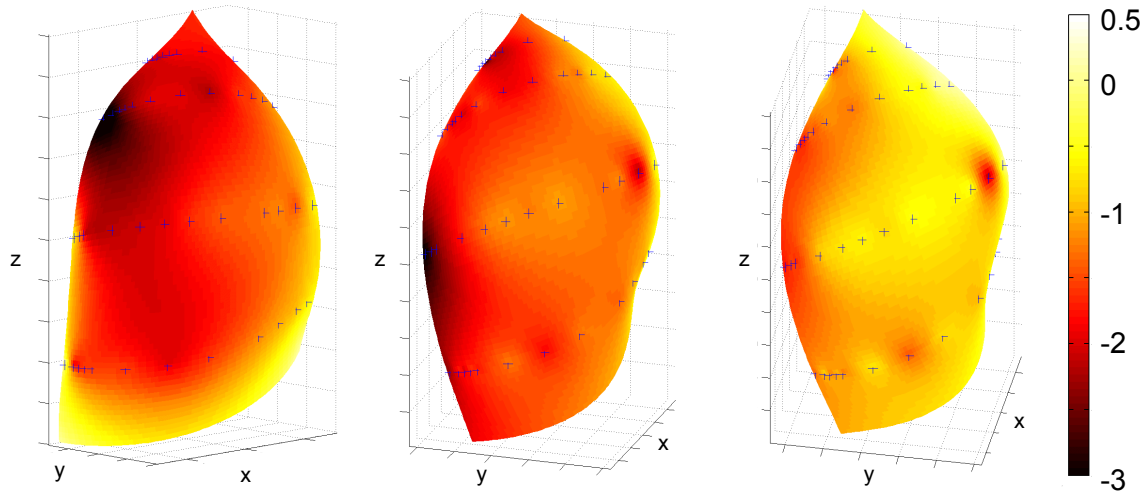
These criteria make it possible to find enough periods for comparison where the conditions do not change too much. The periods were extended in time as long as these criteria were met. In the end, a large range of AWA (between 55° and 140°) is covered by the “stable” periods found, with a certain redundancy for most of the AWA. Each stable period is processed individually.

## AVERAGES AND FLUCTUATIONS

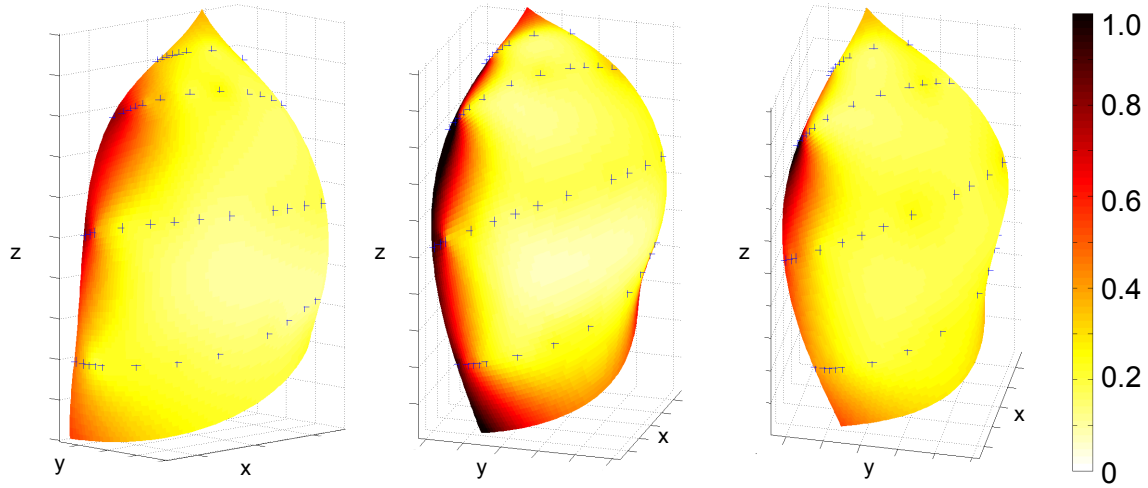
### Pressures

The average pressure distribution and loads are compared according to the apparent wind angle. A large range of AWA was found in a rather constant TWS between 5.8 m/s and 7.1 m/s (11.2 kn to 13.8 kn). The apparent wind angle is measured at the mast head. One should be aware this measurement is affected by the twist of the wind, the upwash effect from the sails and the heel.

To display the pressure distribution on the whole sail from discrete measurement points, a linear Radial Basis Function interpolation was used. On following figures where the pressure distribution is displayed on the spinnaker and blue crosses show where the pressure measurement sensors were located on the sail. Thus pressures at those blue crosses are actual measured values, whereas the pressure distribution is interpolated between the stripes and pressure taps. With no information on the sail boundaries, values at the top (above the stripe



(a) Average



AWA: 66°

AWA: 118°

AWA: 140°

(b) Standard Deviation

**Figure 3. Pressure distributions, time average pressure coefficient  $\Delta C_P$  (a) and the fluctuations (b) for 3 typical AWA (66°, 118°, 140°). Blue crosses show the positions of the pressure taps.**

at 7/8 of the height) and at the bottom (below the stripe at 1/4 of the height) were extrapolated. The shapes used to display the pressure distributions come from other experiments with the same spinnaker where photogrammetric measurements were carried out to acquire the flying shapes (Deparday et al. 2016).

Time-Averaged pressure distributions for similar apparent wind angles have good repeatability. Moreover, the pressure distribution evolves clearly with the AWA. Figure 3a presents three characteristic pressure spatial distributions at 66°, 118° and 140°. It shows the coefficient of the difference of pressure as commonly defined in aerodynamics:

$$\Delta C_P = \frac{P_{\text{leeward}} - P_{\text{windward}}}{\frac{1}{2}\rho(AWS)^2}.$$

At tight angles such as AWA 66°, a bulb of a high suction is found at the leading edge in the top half of the spinnaker ( $\Delta C_P \approx -3$ ) which produces high aerodynamic force.  $\Delta C_P$  on the rest of the sail is around -2 increasing to -1/-0.5 at the trailing edge.

At AWA around 110°-120°, the area where the peak of suction occurs is smaller located about half of the spinnaker height, and the absolute value is lower. On the rest of the spinnaker, the pressure coefficient is rather constant around -1.5 and increasing to -0.5 at the trailing edge.

At AWA 140°, the decrease of suction is even more visible on the whole sail with almost no suction peak at the leading edge and with a reduction of  $|\Delta C_P|$  along the flow up to a positive  $\Delta C_P$  at the trailing edge, even at the actual measured points. A positive pressure coefficient means a collapse of the sail at the trailing edge and thus an unstable flying shape. This is consistent with what the authors have noticed during experiments: at large AWA, the spinnaker starts collapsing first at the leech and not at the luff. However, the time averaged differential pressure measured near the leech is around 4 Pa, which is in the uncertainty of the pressure measurement system. Hence these positive differential pressure values might be slightly negative in reality or are compensated by the tension on the sail.

When the AWA is increased, not only is there a clear decrease of absolute differential pressure coefficient (from -3 down to 0 about), but also a decrease in the AWS (from 7 m/s to 3.5 m/s about). So the absolute values of  $\Delta P$  decrease even more dramatically: at tight AWA, around 65°, the order of magnitude of the differential pressure is -40 Pa, and only -4 Pa at large AWA (-) around 140°).

Figure 3b shows the standard deviation for the corresponding AWA. The standard deviation on the whole sail is interpolated from the standard deviations calculated on the pressure taps only. Higher standard deviations mean bigger variations of pressure during a “stable” period. Despite a clear difference for the pressure distribution on the whole spinnaker depending on the AWA, pressure variations during the “stable” periods have similar spatial patterns. Strong variations are found at the leading edge, around 1, on the whole height for 66° and 118° while the rest of the spinnaker has a standard deviation of about 0.2. However, while the order of magnitude of standard deviation of  $\Delta C_P$  is similar for every AWA, the relative variation of pressures compared with the average pressure coefficient varies. Variations are more significant for large AWA (around 120°-140°) than for tight AWA. For tight AWA, the standard deviation is around 30 Pa (75% of the average pressure). For large AWA, the standard deviation is around 8 Pa (2 times larger than the average pressures).

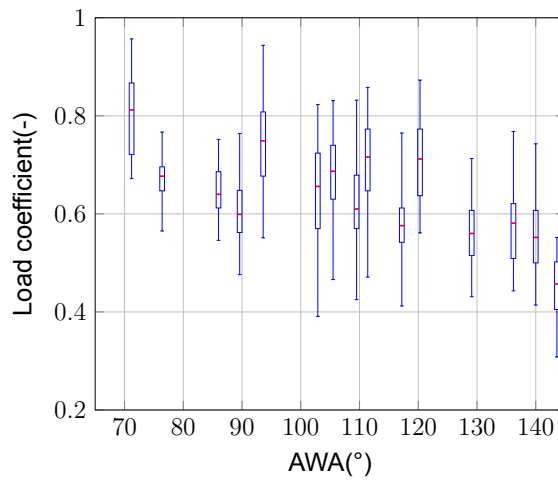
## Loads

Figure 4 displays the load coefficients on the three corners of the spinnaker according to the apparent wind angle:

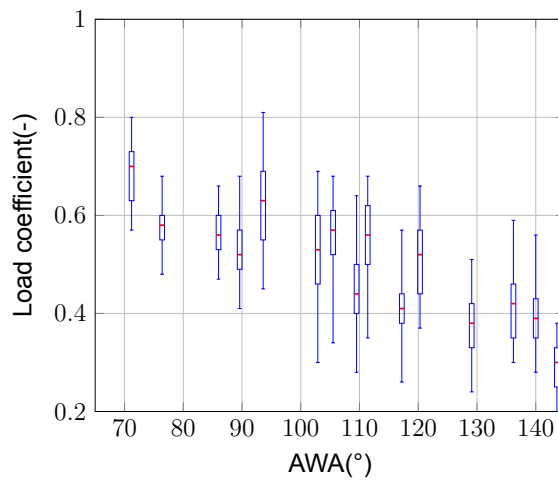
$$C_F = \frac{\text{Load}}{\frac{1}{2}\rho S(\text{AWS})^2} \quad (1)$$

where S is the sail area of the spinnaker and the Load is in Newton.

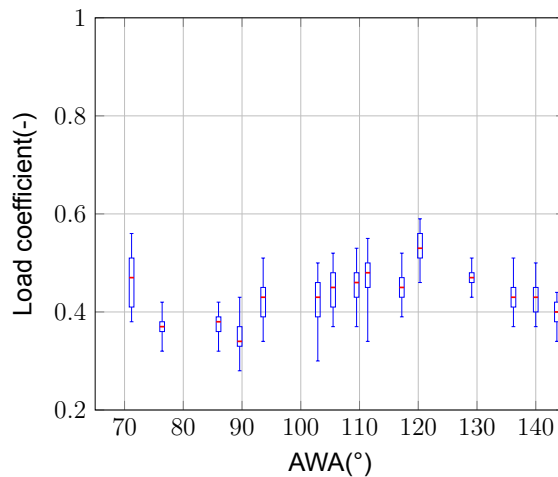
In figure 4, only “stable” periods of 10 seconds minimum are taken. Even though the periods chosen are “stable”, loads can vary significantly. Therefore each period for a specific average apparent wind angle is displayed as a box plot. The central red mark is the median, and the edges of the box are the lower and upper quartile. The lower quartile (Q1) splits off the lowest 25% of data from the highest 75%. The upper quartile (Q3) splits off the highest 25% of loads



**(a) Head coefficient**

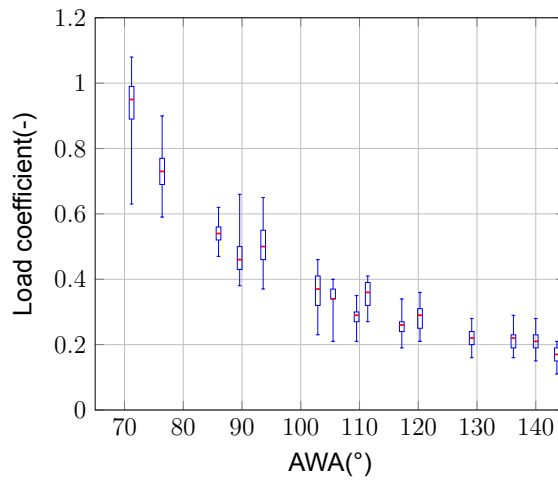


**(b) Tack coefficient**

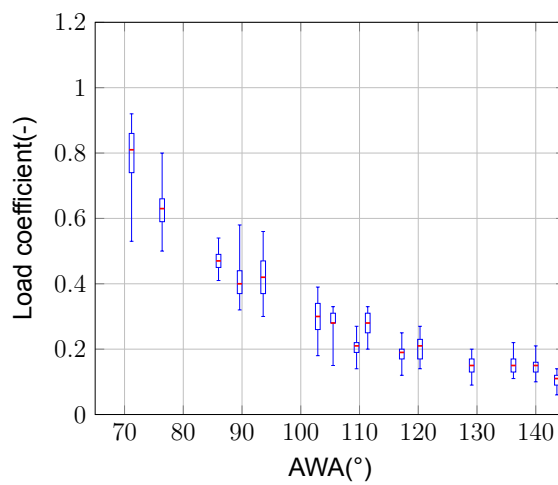


**(c) Clew coefficient**

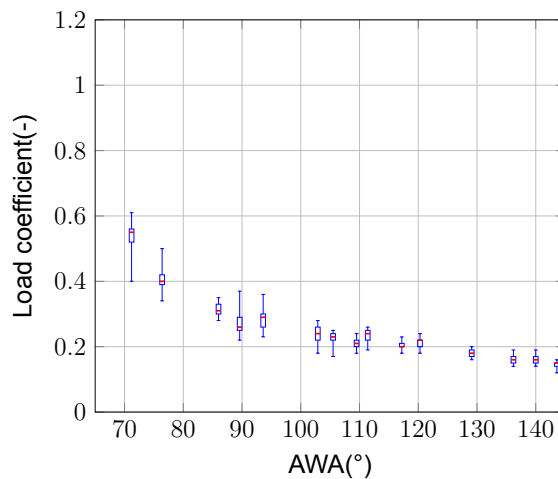
**Figure 4. Boxplot for load coefficients  $C_F$  at the three corners of the spinnaker for different AWA. Central red mark is the median, the box represent the interquartile range between the lower and upper quartiles. It contains 50% of the loads. The upper and lower whiskers indicate the minimum and maximum values.**



**(a) Head coefficient**



**(b) Tack coefficient**



**(c) Clew coefficient**

**Figure 5. Boxplot for load coefficients  $C_F$  with the *TWS* as reference at the three corners of the spinnaker for different AWA. Central red mark is the median, the box represent the interquartile range between the lower and upper quartiles. It contains 50% of the loads. The upper and lower whiskers indicate the minimum and maximum values.**

from the lowest 75%. The box represents the interquartile range (IQR = Q3 –Q1). It contains 50% of the loads recorded during one “stable” period. The whiskers show the maximum and minimum loads recorded.

Figure 4 also shows the general trend of the load coefficients on the three corners according to the apparent wind angle. Head and tack have similar evolution with a decrease especially between 110° and 140° respectively from 0.8 to 0.5 and from 0.7 to 0.3 for the median load coefficients, whereas the clew load coefficient is approximatively constant around 0.4. As explained previously, when the AWA is increased, the AWS decreases. At the clew, the absolute loads decrease mostly due to the decrease of the AWS, whereas at the tack and head, the absolute loads decrease even more significantly. To confirm this, figure 5 displays the evolution of load coefficient using the TWS for the non-dimensional coefficient:

$$C_F = \frac{\text{Load}}{\frac{1}{2}\rho S(\text{TWS})^2} \text{ for figure 5 only,} \quad (2)$$

with the TWS formula from Fossati (2009):

$$\text{TWS} = \sqrt{(\text{AWS} \cos(\text{AWA}) - \text{BS})^2 + (\text{AWS} \sin(\text{AWA}) \cos(\text{heel}))^2}, \quad (3)$$

where the heel is in degree.

TWS is rather constant for every AWA (around 12 kn). A higher change is noticed when the AWA is increased for the head and tack loads than for the clew load which varies a little.

To analyze variations of load coefficients from an aerodynamic point of view the AWS is used for the nondimensional coefficient  $C_F$ . Q3 can be seen as an arbitrary separation between the small variations of loads around the median (inside the IQR) and the peaks of loads (in the top quarter). In figure 4, the IQR has the same relative range for every AWA, between 0% and +10% of the median for the most loaded corners (head and tack) and between -5% and +5% of the median for the clew. Since the IQR is relatively constant and small, one can conclude that for every AWA, without taking into account peaks of loads, the averaged load coefficient is rather stable and varies slightly.

For the most loaded corners (head and tack) the upper whisker (maximum load) is about 20% higher than the median for tight angles ( $\text{AWA} < 100^\circ$ ) and 30% for large angles ( $\text{AWA} > 120^\circ$ ). For the clew point the upper whisker is always about 15% higher than the median for all AWA. Relative variations of loads seem fairly constant for every AWA, and slightly bigger for large AWA at the head and tack points.

It is interesting to note that most variations of loads are present at the head and tack, the closest points of the leading edge where the highest variations of pressure occur. At the clew, the relative variation of loads is smaller.

The variations of loads and pressures are unsteady even during “stable” periods. However specific patterns might be spotted and might be linked to different causes. The yacht motion and its influence on the apparent wind (pitching and rolling of the boat), gusts (pure aerodynamic cause), vortex shedding, or a change of the spinnaker shape as luffing (unsteady fluid-structure interaction) could make the spinnaker forces vary. Therefore, we would like to extract patterns in order to decompose complex pressure evolutions into simpler modes.

These pressure modes could help to describe a temporal global behavior in a better way than analyzing each pressure sensor signal, and could be correlated with other recorded data. We decided to use the Proper Orthogonal Decomposition method to characterize the spatial pattern of pressure variations.

## DECOMPOSITION INTO MODES

### Proper Orthogonal Decomposition method

The Proper Orthogonal Decomposition (POD) (also called Principal Component Analysis, PCA) is based on the Karhunen-Loeve expansion. It was first introduced in the context of Fluid Mechanics by Lumley (1967). The input data  $U(x, t)$  (in our case  $\Delta C_P(x, t)$ ) can be expanded into orthogonal basis functions  $\phi_i(x)$  with time coefficient  $a_n(t)$ :

$$U(x, t) = \sum_n a_n(t) \phi_n(x) \quad (4)$$

As proper modes are derived from the data itself (data driven decomposition), there is no need of a-priori knowledge or education scheme. Moreover, each basis function has its own unique amount of fluctuation energy. These functions are statistically optimal in the least mean-square sense. As a result, fluctuation energy drops down quickly which means a low number of modes is needed in the expansion to reproduce the main variations of the field. POD is a powerful tool for generating lower dimensional models of dynamical systems.

Most of the time, POD is used on the fluctuations of the input data only. After subtracting the average component (seen as the zeroth mode) from the data, a matrix  $U$  is created as a set of  $N$  observations (commonly called snapshots) of  $M$  records. Each column contains all fluctuating input data ( $M$  values) from a specific snapshot and each row contains all snapshots ( $N$  snapshots) from a specific measurement point.

$$U = \begin{bmatrix} u_{11} & u_{12} & \cdots & u_{1N} \\ u_{21} & u_{22} & \cdots & u_{2N} \\ \vdots & \ddots & \ddots & \vdots \\ u_{M1} & u_{M2} & \cdots & u_{MN} \end{bmatrix} \quad (5)$$

Then the auto covariance matrix  $C$  ( $M \times M$ ) is calculated as:

$$C = UU^T \quad (6)$$

because  $M \gg N$ . We have  $M = 44$  measurement points and  $N \approx 20000$ . However in fluid mechanics, it is common to have  $N \gg M$  when using PIV or CFD results for example. For those cases the so-called ‘‘Snapshot POD’’ introduced first by Sirovich (1987) is used. For our experiments, the ‘‘Direct POD’’ has been applied. The corresponding eigenvalue problem of the auto covariance matrix is solved:

$$C\Phi = \lambda\Phi \quad (7)$$

The eigenvectors  $\Phi(i)$  are the POD modes. POD modes are sorted in descending order according to their corresponding eigenvalue  $\lambda(i)$  which represent their energy. The POD mode with the highest corresponding eigenvalue is mode 1. The expansion coefficient (or mode time coefficient) is calculated as follows:

$$\mathbf{a} = \mathbf{U}^T \Phi \quad (8)$$

### POD results

The following results are for a “stable” period with an average AWA of 69°, but are representative to what we have observed for different periods at different AWA. This point will be discussed further in the article. Figure 6 shows the energy distribution for each POD mode. The first mode contains almost 45% of the fluctuation energy. Mode 2 and 3 represent only 15% each, and most of the time other modes have less than 5% of the fluctuation energy. It is clear that the first mode is dominant compared to the others.

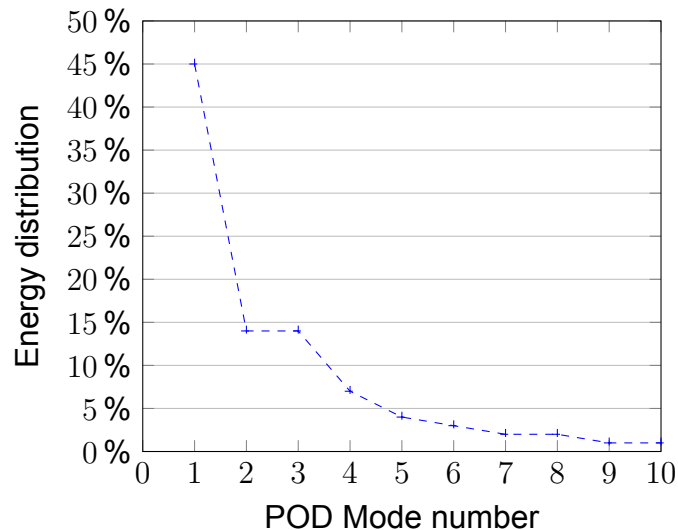


**Figure 6. Energy distribution of the fluctuations for the first 10 modes for AWA 69°.**

The pressure distribution evolution can be simplified by taking only the first terms of the expansion. The reconstruction using the first modes allows us to keep only the most energetic part of the signal and to remove insignificant variations and noise. The precision of the reconstruction has been calculated according to the number of modes. With mode 0 (the average) and mode 1, 85% of the signal is already reconstructed. With 3 modes, the error of reconstruction of the pressure signals is 10%. About 10 modes are required to achieve a reconstruction with less than 5% difference.

Figure 7 presents the first 3 modes. The scale value is arbitrary. To represent a fluctuation of  $C_p$ , they must be multiplied by the corresponding mode time coefficient depending on the time (which can be positive or negative, presented in figure 9). Mode 1 has a bulb of pressure

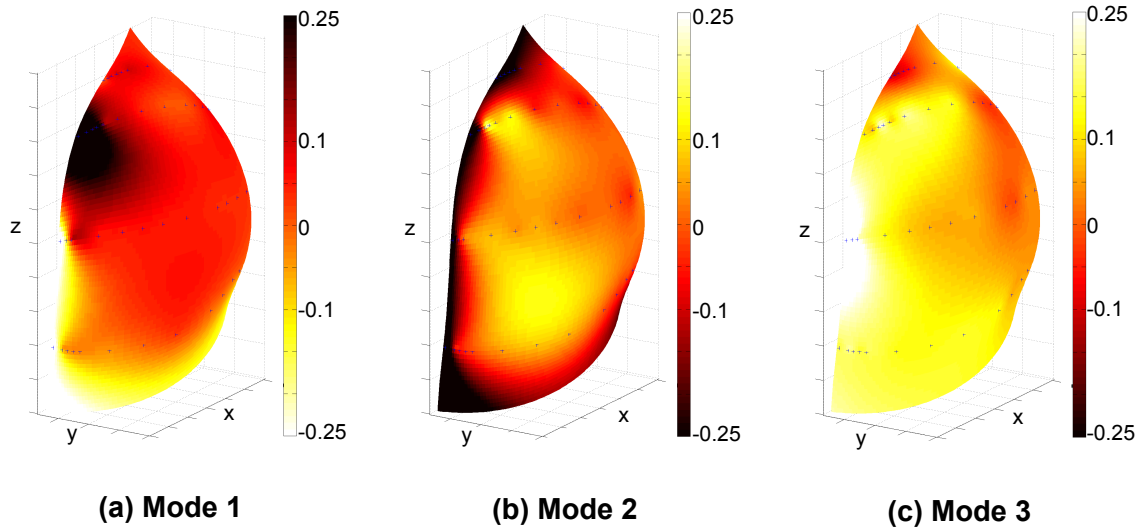


**Figure 7. First 3 spatial orthogonal modes from POD method for AWA 69°. Mode 1 is the most energetic mode.**

on the top half of the spinnaker at the leading edge and a smaller bulb of opposite sign on the bottom half height of the spinnaker. Mode 2 is similar to the standard deviation pattern presented before. Mode 3 and further modes display smaller coherent patterns and may change with the period used.

**Table 1. Energy distribution of the fluctuations for the first 10 modes for different AWA.**

Modes	66 deg	98 deg	120 deg	140 deg
1	43%	46%	45%	45%
2	21%	16%	19%	15%
3	8%	9%	10%	11%
4	7%	6%	6%	7%
5	4%	5%	3%	5%
6	3%	4%	3%	3%
7	2%	3%	2%	2%
8	2%	2%	2%	2%
9	2%	2%	2%	2%
10	1%	1%	1%	1%

Table 1 shows the energy distribution for different “stable” periods at different AWA. The ratio of energy of each mode number is rather constant for every AWA. Moreover, each mode number has a similar pattern of pressure distribution, even though mode 2 and mode 3 are inverted in a few cases.

To compare modes, the maximum value of time coefficient is taken to be multiplied by the spatial mode:  $\max(a_1(t)) \cdot \phi_1(x)$ . Maximum value of time coefficient is used since we want to analyze and compare dominant variations. Moreover, by mathematical definition:  $\forall n, \overline{a_n(t)} = 0$  and thus is irrelevant to be used for comparison. Maximum values of mode 1 for different AWA are presented in figure 8 at 4 different stripes where the pressures are measured (1/4, 1/2, 3/4, 7/8 height of the spinnaker). Differential pressure coefficients have comparable evolution along the curve for every AWA, except that  $|\Delta C_P|$  on the bottom half is slightly smaller for deeper AWA. The bulb of suction at the leading edge at 7/8 and 3/4 of the spinnaker

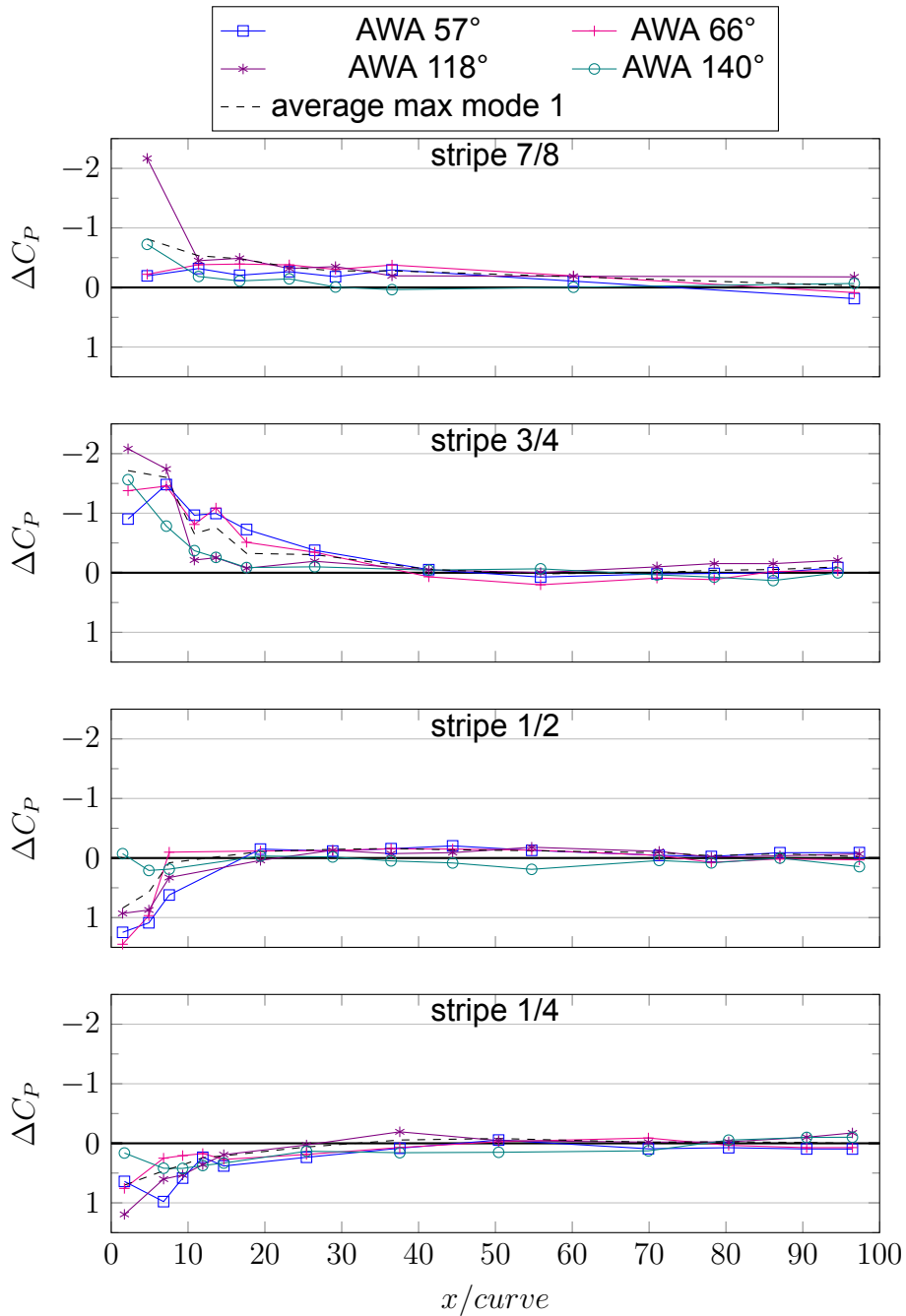


**Figure 8. Mode 1 for maximum time coefficient  $\max(a_1(t) \phi_1(x))$  for different AWA.**

height is always present and a smaller bulb of positive  $\Delta C_P$  at 1/2 and 1/4 height is also spotted. Even if the POD method is a data driven decomposition (i.e. modes are derived from the data itself), there is a good repeatability of POD modes for “stable” periods when the spinnaker has a fixed trim. Moreover mode 1, which plays an important role in the fluctuation of pressures, could be defined as a unique mode whatever the AWA.

POD modes evolve in time. When the time coefficient of a corresponding mode is at an extremum, the corresponding mode is then predominant. Analyzing time coefficients would then help to link pressure variations with other recorded data.

Figure 9 shows the evolution of the time coefficient for the first 3 modes. Amplitudes of mode 1 are larger than the other modes as expected due to the larger energy it possesses. Mode 1 and mode 2 are slightly correlated with a shift between them. A typical pseudo period for

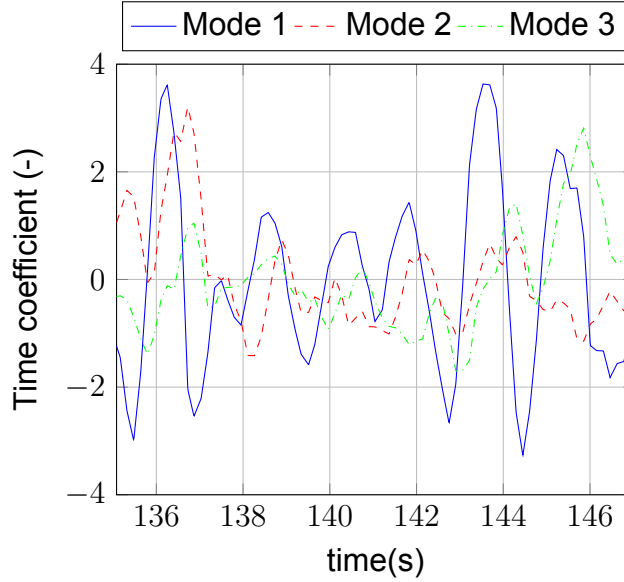


**Figure 9.** Time coefficient  $a_n(t)$  for the first three modes for AWA 69°.

mode 1 stands out for this AWA 69°. Furthermore, for different “stable” periods, at different AWA (not displayed here), similar variations of the temporal coefficient of mode 1 are detected. The dynamics vary with the AWA. A pseudo-period is determined, and the corresponding pseudo-frequency  $f_s$  is displayed in figure 10 (left) according to the corresponding average AWS of the “stable” period. The reduced frequency  $f_r$  shown in figure 10 (right) is calculated as follows:

$$f_r = \frac{f_s \sqrt{S}}{\text{AWS}} \quad (9)$$

with  $S$  the sail area, thus  $\sqrt{S} = 8.3$  m.

When the AWA is increased, the typical pseudo frequency of the time coefficient of mode 1 is reduced proportionally. A linear interpolation passing through the origin can be plotted, hence there is a constant interpolated reduced frequency. There is a linear dependence of the pseudo-frequencies with the AWS. This demonstrates that mode 1 is mostly driven by aerodynamic phenomena and not by mechanical resonance of the rigging or of the membrane of the sail.

In conclusion, the spatial pattern of mode 1 does not change with the AWA, but only the temporal dynamics with an increase of the pseudo-period when the AWA increases (hence when the AWS decreases).

### Application of the POD method on a specific period of flappings

Table 2 presents the cross-correlation of all data measured for the specific period presented in Deparday et al. (2014) where loads and flapping were strongly correlated. The normalized cross-correlation is calculated with the time coefficients of the first three modes. Cross correlation between two signals X and Y is defined as follow:

$$C_{xy}(\tau) = \mathcal{E}[(X(t_2) - \mu_{X(t_2)}) - (Y(t_1) - \mu_{Y(t_1)})] \quad (10)$$

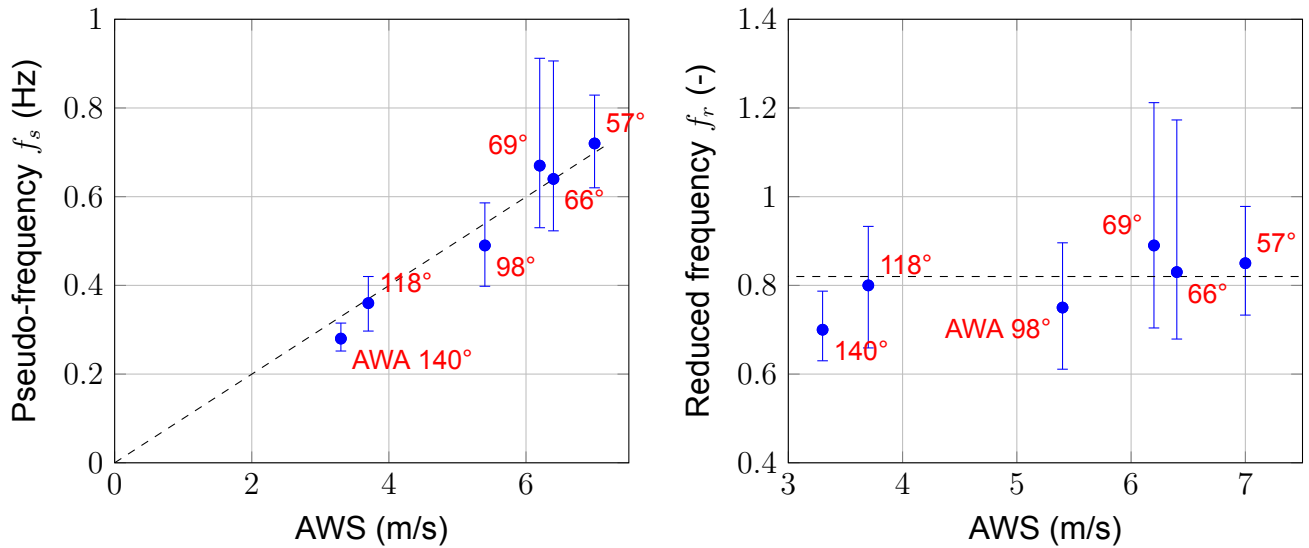


**Figure 10. Pseudo-frequency (left) and reduced frequency (right) of the time coefficient of the first POD mode (blue dots) for different AWA as a function of the AWS. A linear interpolations fit the experimental data.**

**Table 2. Cross-correlation between different signals recorded during experiments, and first 3 modes of the POD. Correlation values (and their corresponding colors) vary between 0 (in white) meaning no correlation and 1 (in red), same dynamics.**

	forestay	backstay	V1 windw'd	D1 windw'd	D1 leew'd	Head	Tack	Clew	mode 1	mode 2	mode 3	roll	pitch	yaw	AWA	AWS	BS
forestay	1.00	0.58	0.62	0.63	0.78	0.59	0.59	0.59	0.65	0.62	0.59	0.60	0.69	0.51	0.73	0.59	0.40
backstay	0.58	1.00	0.88	0.92	0.62	0.96	0.95	0.93	0.91	0.66	0.45	0.58	0.61	0.75	0.58	0.49	0.57
V1 windw'd	0.62	0.88	1.00	0.99	0.79	0.94	0.94	0.94	0.85	0.66	0.41	0.48	0.61	0.68	0.63	0.50	0.44
D1 windw'd	0.63	0.92	0.99	1.00	0.79	0.95	0.95	0.95	0.88	0.68	0.41	0.54	0.61	0.71	0.63	0.54	0.46
D1 leew'd	0.78	0.62	0.79	0.79	1.00	0.69	0.70	0.76	0.66	0.53	0.52	0.49	0.52	0.65	0.60	0.54	0.44
Head	0.59	0.96	0.94	0.95	0.69	1.00	1.00	0.98	0.90	0.63	0.47	0.58	0.57	0.71	0.63	0.53	0.57
Tack	0.59	0.95	0.94	0.95	0.70	1.00	1.00	0.98	0.88	0.61	0.45	0.54	0.55	0.71	0.62	0.51	0.58
Clew	0.59	0.93	0.94	0.95	0.76	0.98	0.98	1.00	0.85	0.65	0.44	0.63	0.58	0.70	0.67	0.61	0.60
mode 1	0.65	0.91	0.85	0.88	0.66	0.90	0.88	0.85	1.00	0.72	0.43	0.52	0.63	0.74	0.54	0.47	0.38
mode 2	0.62	0.66	0.66	0.68	0.53	0.63	0.61	0.65	0.72	1.00	0.46	0.64	0.84	0.60	0.68	0.48	0.29
mode 3	0.59	0.45	0.41	0.41	0.52	0.47	0.45	0.44	0.43	0.46	1.00	0.66	0.41	0.45	0.56	0.75	0.51
roll	0.60	0.58	0.48	0.54	0.49	0.58	0.54	0.63	0.52	0.64	0.66	1.00	0.83	0.83	0.77	0.88	0.47
pitch	0.69	0.61	0.61	0.61	0.52	0.57	0.55	0.58	0.63	0.84	0.41	0.83	1.00	0.76	0.85	0.68	0.28
yaw	0.51	0.75	0.68	0.71	0.65	0.71	0.71	0.70	0.74	0.60	0.45	0.83	0.76	1.00	0.66	0.56	0.46
AWA	0.73	0.58	0.63	0.63	0.60	0.63	0.62	0.67	0.54	0.68	0.56	0.77	0.85	0.66	1.00	0.58	0.52
AWS	0.59	0.49	0.50	0.54	0.54	0.53	0.51	0.61	0.47	0.48	0.75	0.88	0.68	0.56	0.58	1.00	0.50
BS	0.40	0.57	0.44	0.46	0.44	0.57	0.58	0.60	0.38	0.29	0.51	0.47	0.28	0.46	0.52	0.50	1.00

where  $\mathcal{E}[\cdot]$  is the expected value operator,  $\tau = t_2 - t_1$  is the shift applied between two signals.  $\mu_X$  and  $\mu_Y$  are the mean functions.

The cross correlation matrix is calculated to determine the correlations of every signal with each other. The values are between 0 when not correlated at all (in white in the table) and 1 when signals have the same dynamics (in red in the table). Colors in Table 2 highlight the correlations between experimental data. The diagonal represents the auto-correlation of every signal.

A very strong correlation is present between the loads except with the forestay and the shroud D1 leeward as they are not loaded and slack. The time coefficient of mode 1 is also well correlated with the loads (around 0.9). There is no delay between mode 1 and the spinnaker aerodynamic loads, and the spinnaker aerodynamic loads are 0.1 s in advance of the standing rigging loads. In this case the pressure evolution is instantaneously transmitted to the corners of the spinnaker which then transmit this increase of loads to the shrouds and backstay. Mode 1 is a good parameter to define peaks of loads due to flapping of the spinnaker. Here mode 2 is reasonably correlated with mode 1 with a coefficient of 0.72. The shift between the two modes is 0.4 s. For this “stable” period, the pseudo-period is around 1.5 s. The average shift between the two time coefficients is therefore about a quarter of a pseudo-period ( $0.4/1.5 = 0.27$ ). The average shift calculated is indeed between the phase shift measured at the maxima of the modes ( $1/6-1/5$  of a pseudo period) and at the phase shift found at their minima ( $1/3-1/2$  of a pseudo period). This pseudo-period corresponds to what was presented in Deparday et al. (2014). To describe the expansion of the high suction towards the leading edge and the propagation of the flapping, as presented in Deparday et al. (2014), the addition of mode 2 is necessary.

Loads are also slightly correlated with the yaw. The shift between the two signals is about 1 second in advance for the loads. A peak of aerodynamic loads might modify the aerodynamic center of effort and thus change the equilibrium of the sailing yacht and make the course vary.

In conclusion, the POD method makes it possible to describe a global temporal behavior of pressures in a better way than analyzing each pressure sensor signal. It can be compared as a unique signal with the other measurement data. It confirms that flapping prevails in the fluctuations of the corner loads.

## CONCLUSIONS

Full-Scale experiments were carried out on an instrumented J/80 sailing yacht where loads, pressure distribution on the spinnaker, boat and wind data were measured at different downwind angles. We show pressure coefficients and load coefficients decrease when the AWA is increased, whereas variations of load and pressure coefficients are mainly constant. Therefore variations relative to the average loads or pressures are bigger for larger AWA. Moreover we found that most of the pressure and load variations are mainly at the luff for every AWA.

This paper presented a way to characterize the pressure evolution due to flapping. A POD analysis has been used on pressure signals in order to identify the most energetic patterns. Mode 1 which represents almost half of the fluctuation energy describes well the flapping of the luff. The spatial pattern of mode 1 of the differential pressure coefficients does not change with the AWA. It can be represented as a unique spatial pattern for all AWA. The variations of pressures due to the flapping are therefore proportional to the square of the AWS. Furthermore, the dynamics of POD mode 1 evolves with the AWA. For each AWA, a typical pseudo-period is noticed. It decreases linearly with the AWS. It proves the flapping

phenomenon is not a random fluctuation but is an almost periodical behavior, an intrinsic instability of the spinnaker in certain conditions.

The addition of mode 2 is necessary to describe the propagation of this flapping at a different height of the sail and the expansion of the high suction towards the leading edge.

POD enables the characterisation of a global unsteady behavior instead of analyzing all local pressure time series. It shows sail designers where the highest variations of pressure occur when flapping. Furthermore, the first modes allow reconstruction of a signal with the main variations (i.e. with the most energetic part) and remove noises. Therefore comparison with other measurements or numerical simulations is simplified.

## Acknowledgments

This project has received funding from the European Union's Seventh Programme for research, technological development and demonstration under grant agreement No PIRSES-GA-2012-318924, and from the Royal Society of New Zealand for the UK-France-NZ collaboration project SAILING FLUIDS.

## REFERENCES

- Augier, B., Bot, P., Hauville, F., and Durand, M. (2012). "Experimental validation of unsteady models for fluid structure interaction: Application to yacht sails and rigs". In: *Journal of Wind Engineering and Industrial Aerodynamics*, 101, pp. 53–66.
- Augier, B., Hauville, F., Bot, P., Aubin, N., and Durand, M. (2014). "Numerical study of a flexible sail plan submitted to pitching: Hysteresis phenomenon and effect of rig adjustments". In: *Ocean Engineering*, 90, pp. 119–128.
- Campbell, I. M. C. (2014a). "Comparison of downwind sailing performance predicted from wind tunnel tests with full-scale trials from America's Cup class yachts". In: *23rd HISWA Symposium on Yacht Design and Yacht Construction*.
- Campbell, I. M. C. (2014b). "A comparison of downwind sail coefficients from tests in different wind tunnels". In: *Ocean Engineering*, 90, pp. 62–71.
- Chapin, V. G., Carlan, N. de, and Heppel, P. (2011). "A Multidisciplinary Computational Framework for Sailing Yacht Rig Design & Optimization through Viscous FSI". In: *20th Chesapeake Sailing Yacht Symposium*. March. Annapolis, pp. 1–17.
- Deparday, J., Bot, P., Hauville, F., Augier, B., and Rabaud, M. (2016). "Full-scale flying shape measurement of offwind yacht sails with photogrammetry". In: *Ocean Engineering*, 127. November 2016, pp. 135–143. ISSN: 00298018.
- Deparday, J., Bot, P., Hauville, F., Motta, D., Le Pelley, D. J., and Flay, R. G. J. (2014). "Dynamic measurements of pressures, sail shape and forces on a full-scale spinnaker". In: *23rd HISWA Symposium on Yacht Design and Yacht Construction*. Amsterdam.
- Durand, M., Leroyer, A., Lothodé, C., Hauville, F., Visonneau, M., Floch, R., and Guillaume, L. (2014). "FSI investigation on stability of downwind sails with an automatic dynamic trimming". In: *Ocean Engineering*, 90, pp. 129–139. DOI: 10.1016/j.oceaneng.2014.09.021.
- Flay, R. G. J. (1996). "A twisted flow wind tunnel for testing yacht sails". In: *Journal of Wind Engineering and Industrial Aerodynamics*, 63.1-3, pp. 171–182.

- Fossati, F., Bayati, I., Orlandini, F., Muggiasca, S., Vandone, A., Mainetti, G., Sala, R., Bertorello, C., et al. (2015). "A novel full scale laboratory for yacht engineering research". In: *Ocean Engineering*, 104, pp. 219–237.
- Fossati, F. (2009). *Aero-hydrodynamics and the performance of sailing yachts*. International Marine / Mc Graw Hill.
- Graf, K. and Müller, O. (2009). "Photogrammetric Investigation of the Flying Shape of Spinnakers in a Twisted Flow Wind Tunnel". In: *19th Chesapeake Sailing Yacht Symposium*. March. Annapolis.
- Hansen, H., Jackson, P., and Hochkirch, K. (2002). "Comparison of Wind Tunnel and Full-Scale Aerodynamic Sail Force measurements". In: *High Performance Yacht Design Conference*. Auckland.
- Herman, J. S. (1989). "A sail force dynamometer: design, implementation and data handling". PhD thesis. Massachusetts Institute of Technology, p. 52.
- Hochkirch, K. and Brandt, H. (1999). "Fullscale hydrodynamic force measurement on the Berlin sailing dynamometer". In: *14th Chesapeake Sailing Yacht Symposium*. Annapolis, pp. 33–44.
- Le Pelley, D. J., Morris, D., and Richards, P. (2012). "Aerodynamic force deduction on yacht sails using pressure and shape measurements in real time". In: *4th High Performance Yacht Design Conference*. Auckland, pp. 28–37.
- Le Pelley, D. J. and Richards, P. (2011). "Effective Wind Tunnel Testing of Yacht Sails Using a Real-Time Velocity Prediction Program". In: *20th Chesapeake Sailing Yacht Symposium*. Annapolis.
- Le Pelley, D. J., Richards, P. J., and Berthier, A. (2015). "Development of a directional load cell to measure flying sail aerodynamic loads". In: *5th High Performance Yacht Design Conference*. Auckland, pp. 66–75.
- Lombardi, M., Cremonesi, M., Giampieri, A., and Parolini, N. (2012). "A strongly coupled fluid-structure interaction model for wind-sail simulation". In: *4th High Performance Yacht Design Conference*. Auckland, pp. 212–221.
- Lozej, M., Golob, D., and Bokal, D. (2012). "Pressure distribution on sail surfaces in real sailing conditions". In: *4th High Performance Yacht Design Conference*. Auckland, pp. 242–251.
- Lumley, J. L. (1967). "The structure of inhomogeneous turbulence". In: *Atmospheric Turbulence and Wave Propagation*. Ed. by A. Yaglom and V. Tatarski. Moscow: Nauka, pp. 166–178.
- Masuyama, Y. (2014). "The work achieved with the sail dynamometer boat "Fujin", and the role of full scale tests as the bridge between model tests and CFD". In: *Ocean Engineering*, 90, pp. 72–83.
- Motta, D., Flay, R. G. J., Richards, P. J., Le Pelley, D. J., Deparday, J., and Bot, P. (2014). "Experimental investigation of asymmetric spinnaker aerodynamics using pressure and sail shape measurements". In: *Ocean Engineering*, 90, pp. 104–118.

- Motta, D., Flay, R. G. J., Richards, P., Le Pelley, D. J., Bot, P., and Deparday, J. (2015). "An investigation of the dynamic behaviour of asymmetric spinnakers at full-scale". In: *5th High Performance Yacht Design Conference*. Auckland, pp. 76–85.
- Ranzenbach, R., Armitage, D., and Carrau, A. (2013). "Mainsail Planform Optimization for IRC 52 Using Fluid Structure Interaction". In: *21st Chesapeake Sailing Yacht Symposium*. March. Annapolis, pp. 50–58.
- Renzsch, H. and Graf, K. (2010). "Fluid Structure Interaction Simulation of Spinnakers—Towards Simulation Driven Sail Design". In: *21st HISWA Symposium on Yacht Design and Yacht Construction*.
- Renzsch, H. and Graf, K. (2013). "An experimental validation case for fluid-structure-interaction simulations of downwind sails". In: *21st Chesapeake Sailing Yacht Symposium*. March. Annapolis, pp. 59–66.
- Sirovich, L. (1987). "Turbulence and the dynamics of coherent structures part i: coherent structures". In: *Quarterly of Applied Mathematics*, XLV.3, pp. 561–571.
- Trimarchi, D., Vidrascu, M., Taunton, D., Turnock, S., and Chapelle, D. (2013). "Wrinkle development analysis in thin sail-like structures using MITC shell finite elements". In: *Finite Elements in Analysis and Design*, 64, pp. 48–64.
- Viola, I. M., Biancolini, M. E., Sacher, M., and Cella, U. (2015). "A CFD-based wing sail optimisation method coupled to a VPP". In: *5th High Performance Yacht Design Conference*. Auckland, pp. 1–7.
- Viola, I. M. and Flay, R. G. J. (2011). "Sail pressures from full-scale, wind-tunnel and numerical investigations". In: *Ocean Engineering*, 38.16, pp. 1733–1743.
- Viola, I. M. and Flay, R. G. J. (2012). "Sail Aerodynamics: On-Water Pressure Measurements on a Downwind Sail". In: *Journal of Ship Research*, 45.4, pp. 197–206.
- Zasso, A., Fossati, F., and Viola, I. M. (2005). "Twisted Flow Wind Tunnel Design for Yacht Aerodynamic Studies". In: *EACWE4 - The 4th European & African Conference on Wind Engineering*. Prague, pp. 1–14.